

System-level modeling and simulation of biochemical assays in lab-on-a-chip devices

Yi Wang · Aditya S. Bedekar · S. Krishnamoorthy · Sachin S. Siddhaye · Shivshankar Sundaram

Received: 22 June 2006 / Accepted: 20 August 2006 / Published online: 21 November 2006
© Springer-Verlag 2006

Abstract We present a “mixed-methodology” based system-level modeling and simulation for biochemical assays in lab-on-a-chip (LoC) devices. The methodology uses a combination of numerical schemes and analytical approaches to simulate biological and physicochemical processes, specifically, an integral approach for fluid flow and electric field, method of lines (MOL) and two-compartment models for biochemical reactions, and Fourier series-based model for analyte mixing. The solution procedure begins with decomposing the LoC device into a system of inter-connected components (e.g., channels and junctions) and the models are solved in a network fashion. Models are developed to accurately capture the multi-physics (e.g., flow, mixing, and reaction) behavior of individual components. The assembly of the components is facilitated via exchange of fluid flux and Fourier series coefficients (or average concentration) of analytes between various components, which enables network solution of the models. The system models are validated against both experimental and numerical models on various biochemical assays (e.g. immunoassays and enzymatic reactions), showing significant computational speedup (100–10,000-fold depending on the assay) without appreciably compromising accuracy (<10% error relative to numerical analysis).

Keywords Modeling · Simulation · Lab-on-a-chip · Biochemical assay

1 Introduction

Lab-on-a-chip (LoC) systems hold a great promise for a variety of applications in biology, medicine, and chemistry (Aouroz et al. 2002; Reyes et al. 2002). The advantages include speedup in analysis time, savings in reagents and samples, improved throughput, and capability of implementing high levels of integration and automation. Multi-physics phenomena and the continuously growing integration level of LoC systems increase the complexity and difficulty of chip design. Although high fidelity (3D) numerical simulations enable a coupled spatio-temporal analysis of these phenomena, use of these tools for the system-level analysis is computationally expensive, leading to long turnaround times. The application of these techniques has therefore been limited primarily to component-level design. To overcome their limitations, efficient-parameterized modeling and system-level simulation approaches to enable rapid design evaluation are being actively pursued. Zhang et al. developed an integrated modeling and simulation framework for microfluidic systems in SystemC to evaluate and compare the performance of a polymerase chain reaction (PCR) in continuous-flow and droplet-based microfluidic systems (Zhang et al. 2004). However, their approach to system-level representation and implementation relies on the availability of component models from numerical simulations or experimental data. Chatterjee et al. assembled circuit/device models to analyze fluidic transport, chemical reaction, reagent mixing, as well as separation in integrated microfluidic systems (Chatterjee and Aluru 2005). To achieve a fast simulation speed, microfluidic reactors are described

Y. Wang (✉) · A. S. Bedekar · S. Krishnamoorthy · S. S. Siddhaye · S. Sundaram
CFD Research Corporation, 215 Wynn Drive,
Huntsville, AL 35805, USA
e-mail: yxw@cfdr.com

using a “continuous stirred tank reactor” (CSTR) model. The transport phenomena and the non-uniformity of concentration within the reactor are neglected. Practically, this treatment may be inadequate, as microfluidic assays are typically characterized by laminar flow and slow diffusion-based mixing (Wang et al. 2005a). More recently, Wang et al. have developed a behavioral modeling and schematic simulation environment based on LoC system hierarchy in Verilog-A to investigate an integrated multi-functional (mixing, reaction, injection, and separation) competitive immunoassay microchip. The reaction model studied was limited to a transported-limited immunoassay that allowed a decoupled treatment of mixing and biochemical reactions (Wang et al. 2005b). A common issue existing in prior investigations is the insufficient consideration of the coupling between the transport phenomena and biochemical reaction that is important for accurate system-level simulation of microfluidic assays.

To address this issue, we will present a “mixed-methodology” based system-level simulation of LoC devices, in which numerical schemes and analytical approaches are integrated in a single simulation engine to accurately capture the different multi-physics behavior of each assay component as well as their overall effects on LoC system performance. The underlying philosophy of our methodology is the predominant use of fast and efficient analytical models, along with a selective use of numerical models for components that do not allow for analytical treatment. Specifically, we use a two-compartment model for describing surface (heterogeneous) biochemical assays, and the method of lines (MOL) for volumetric (homogeneous) assays. They are integrated with analytical models for analyte mixing and buffer fluid flow in both pressure-driven and electrokinetic flow. A strategy to enable system-level simulation by exchange of information between components described by these disparate models is also implemented. The paper is organized as follows: we will first consider the system-level representation of LoC devices in Sect. 2. A description of the component models is given in Sect. 3. The system-level model is described in Sect. 4, while Sect. 5 illustrates the application of system-level models to various LoC systems with integrated biochemical assays. The simulation results are validated by comparison with numerical analysis and experimental data. The paper concludes with a summary and possible direction for future work in Sect. 6.

2 A schematic representation of lab-on-a-chip systems

For a system-level solution, a LoC system is represented as a network of components connected by edges. The edges can be considered as “wires” of zero resistance that exchange the information of flow rate, electric current, and analyte concentration between components. Our formulation does not restrict the number of edges emanating from a component. However, two components are connected uniquely by an edge. The network representation is illustrated by the enzyme assay chip (Schilling et al. 2002) shown in Fig. 1a, which consists of a network of various components including channels (L1–L6), volumetric reactors (VR1, VR2), T junctions (T1–T3), and wells (W1–W5) as shown in Fig. 1b. Further the T junctions can be classified as “mergers” (T1, T3) or “splitters” (T2) depending on the direction of branch and main flows.

3 Model formulation

We present the governing equations and model formulation for pressure-driven and electrokinetic flow, as well as analyte transport in LoC systems. We assume the following for the microfluidic channel in Fig. 2, where x , y , and z are the channel’s axial, cross-stream, and depth-wise coordinates, respectively; L , w and h are the length, width, and depth of the channel.

1. Flow or electric field is at steady state.
2. The buffer solution is assumed Newtonian and incompressible, electrically neutral, and with constant electrical conductivity and viscosity.
3. Analyte concentration is dilute, i.e., the effects of analyte concentration on surface charges and buffer properties (e.g., viscosities and electrical conductivity) are assumed negligible (Coelho et al. 2005; Cummings et al. 2000; Ermakov et al. 1998; Holden et al. 2003; Kamholz et al. 1999).
4. The pressure and electric fields are assumed to be completely decoupled (Ajdari 2004; Xuan and Li 2004). For electrokinetic flow, the similitude between the electrokinetic flow and electric field holds (Cummings et al. 2000). This implies that the electrokinetic velocity of the analyte is parallel to the external electric field (Cummings et al. 2000; Wang et al. 2005a) (i.e., $u = vE$, v is the electrokinetic mobility of the analyte).
5. The channel cross section is uniform and the flow is fully developed. In addition, the channel aspect ratio $\beta = w/h$ is large when pressure-driven flow is considered.

Fig. 1 **a** A LoC device for cell lysis, extraction, reaction, and detection of intracellular components (Schilling et al. 2002). **b** Schematic representation of component network describing the device

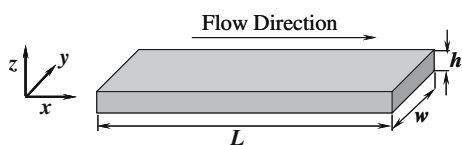
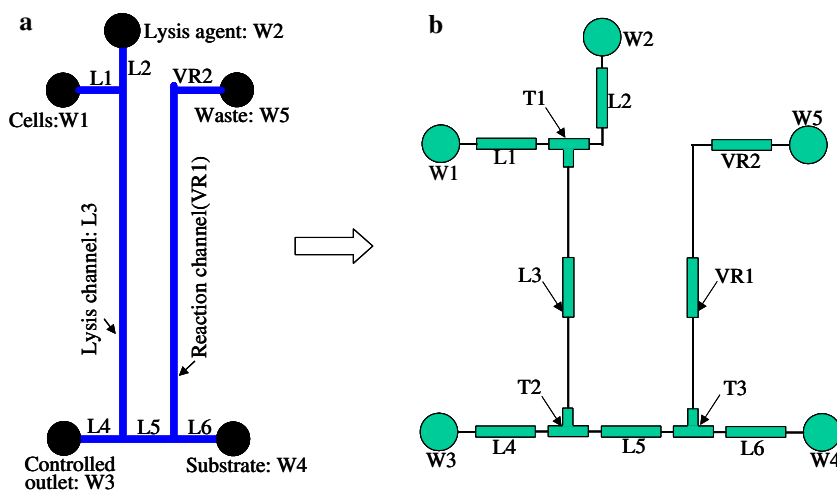


Fig. 2 Geometry of a microchannel and its coordinate definition

Based on these assumptions, the governing equation for pressure-driven flow is the steady-state Navier–Stokes equation:

$$\mu \nabla^2 u - \frac{dP}{dx} = 0 \tag{1}$$

where u is the axial buffer flow velocity, P is the pressure, and μ is the dynamic viscosity of the buffer. An analytical solution (White 1991) to Eq. 1 yields the fluidic resistance that relates the pressure drop ΔP across the channel to its volumetric flow rate q :

$$R = \frac{\Delta P}{q} = \frac{12\beta L \mu}{w^4 \left[1 - \frac{192\beta}{\pi^5} \sum_{i=1,3,5,\dots}^{\infty} \frac{\tanh(i\pi/2\beta)}{i^5} \right]} \tag{2}$$

where $q = \int_0^h \int_0^w u \, dy \, dz$. Similar relations are available for channels of other cross sections (White 1991).

The electric field driving electro-osmotic flow is described by the Laplace equation (based on electro-neutrality assumption in the bulk fluid):

$$\nabla^2 \phi = 0 \tag{3}$$

where ϕ is the electric potential. The electric field then is given by $E = -\nabla \phi = -\Delta \phi / L$. Thus, in terms of the buffer’s electric conductivity σ , the electric resistance R_{Elec} of the channel that relates the potential drop $\Delta \phi$ and the electric current I is given by (Wang et al. 2006b)

$$R_{Elec} = \frac{\Delta \phi}{I} = \frac{L}{\sigma w h} \tag{4}$$

In Eq. 4, we neglect the convection current. The axial analyte velocity can then be explicitly determined by $u = vE$ (assumption 4), where v is the algebraic sum of the buffer’s electroosmotic mobility and analyte’s electrophoretic mobility in the buffer (Wang et al. 2005a).

Analyte transport is described by the generalized convection–diffusion equation in pressure-driven and electrokinetic flow and written as

$$\frac{\partial c_i}{\partial t} + u_i \frac{\partial c_i}{\partial x} - D_i \left(\frac{\partial^2 c_i}{\partial x^2} + \frac{\partial^2 c_i}{\partial y^2} + \frac{\partial^2 c_i}{\partial z^2} \right) - R_i = 0 \tag{5}$$

where t denotes the time. The subscript i represents the quantities associated with the i th analyte in the buffer stream, u is the analyte migration velocity, and D is the diffusivity. R is the volumetric reactive source term and depends on the reaction mechanism. As the flow is fully developed along axial channel length, the convective terms for y and z directions are neglected.

In this paper, we will investigate volumetric and surface reaction-based biochemical assays in LoC devices. In volumetric reaction-based assays, two streams carrying different analytes merge into another channel where they inter-diffuse and react in the entire channel volume. The variations in cross-stream concentration profiles of analytes and/or reaction products resulting from diffusion-based mixing, sample splitting and merging, as well as reaction whose rate depends on local concentrations are in steady state. However, in surface reaction-based assays, analytes flow through the channel and react with receptors immobilized on the bottom channel surface. Therefore, transient behavior (rather

than the spatial distribution) of analyte concentration in association and disassociation phases is of primary importance in the study of biomolecular interactions. For this reason, two distinctly different sets of models that, respectively, predict *steady-state cross-stream* concentration profiles in volumetric assays (Sect. 3.1) and *transient cross-sectional average* concentration in surface assays (Sect. 3.2) will be developed.

3.1 Volumetric biochemical reaction-based assays

In volumetric reaction-based assays, cross-stream concentration profiles of analytes are affected by mixing, splitting, merging, and reactions. In this section, we describe governing convection–diffusion phenomena in the microfluidic components for such assays.

3.1.1 Mixer

To estimate the steady-state analyte mixing in microfluidic channels, we neglect the terms associated with transient variation, axial and depth-wise diffusion [by invoking assumptions 1 and 5 (Coelho et al. 2005; Holden et al. 2003; Kamholz et al. 1999; Wang et al. 2006c)], and reactive source term. Equation 5 can therefore be written as

$$U_i \frac{\partial c_i}{\partial x} = D_i \frac{\partial^2 c_i}{\partial y^2} \quad (6)$$

where U is the average analyte velocity. Note that for pressure-driven flow, Eq. 6 only holds for channels with large aspect ratios ($\beta \gg 1$) (Coelho et al. 2005; Holden et al. 2003; Kamholz et al. 1999; Wang et al. 2006c). The analyte flux at the channel walls is assumed to be zero, i.e. $(\partial c_i / \partial y)|_{y=0,w} = 0$. Based on this, a generalized solution to Eq. 6, yielding the analyte concentration profile at any axial position x ,

$$c_i(x, \eta) = \sum_{n=0}^{\infty} d_{i,n}^{(\text{in})} e^{-(n\pi)^2 x D_i / (U_i w^2)} \cos(n\pi\eta) \quad (7)$$

where $\eta = y/w$ ($0 \leq \eta \leq 1$) is the normalized cross-stream coordinate, $d_{i,n}^{(\text{in})}$ are the n th Fourier cosine series coefficients (Wang et al. 2005a, 2006b) of the analyte concentration profile at the channel inlet and are given by $c_i(x=0, \eta) = c_i^{(\text{in})}(\eta) = \sum_{n=0}^{\infty} d_{i,n}^{(\text{in})} \cos(n\pi\eta)$. Set $x = L$ in Eq. 7, we obtain the analyte concentration profile at the channel outlet by

$$c_i(x=L, \eta) = c_i^{(\text{out})}(\eta) = \sum_{n=0}^{\infty} d_{i,n}^{(\text{out})} \cos(n\pi\eta) \quad (8)$$

and $d_{i,n}^{(\text{out})} = d_{i,n}^{(\text{in})} e^{-(n\pi)^2 \tau_i}$

where $d_{i,n}^{(\text{out})}$ are the Fourier series coefficients of the concentration profile at the outlet and $\tau_i = (L/w)/Pe_i$ is the ratio of time scales associated with axial convection to cross-stream diffusion and $Pe_i = wU_i/D_i$ is the Peclet number of the i th analyte, a ratio of the axial convective rate to the cross-stream diffusive rate. Equation 8 correlates the Fourier cosine series coefficients $d_{i,n}$, at the channel inlet and outlet. Thus, $d_{i,n}$ can be used to transfer information about the analyte concentration profile from one component to another within the network (Sect. 4).

For junctions where analyte streams merge (e.g. a T junction), the analyte concentration profile at its outlet can be treated as a cross-stream superposition of the upstream profiles. In contrast, the splitting junction splits the incoming analyte stream as well as its concentration profile into two branches. A brief description of the models that relate the Fourier coefficients $d_{i,n}$ of analyte concentrations at inlets and outlets in these components is given in Appendix A. More details are discussed elsewhere (Wang et al. 2005a, 2006b). In addition, chaotic secondary flows in junctions could be induced at high Reynolds number, e.g., $Re \sim 100$ (Bothe et al. 2006). Hence, models for mixers, mergers, and splitters are valid for low Reynolds regimes ($Re \ll 100$), where laminar diffusion dominates (Wang et al. 2005a; 2006c).

3.1.2 Volumetric reactor

The governing equation for volumetric reactions in microfluidic channels is derived based on the same assumptions for Eq. 6. The key difference is the inclusion of the reactive source term R_i describing consumption or generation of the analyte as a result of the reaction. Since R_i is generally nonlinear and does not allow for an analytical solution, we use the MOL (Wouwer et al. 2004) to obtain the solution of cross-stream analyte concentration profiles. Specifically, using a central difference scheme, the discretized form of the governing equation can be written as

$$U_i \frac{\partial c_i^j}{\partial x} = D_i \frac{c_i^{j-1} - 2c_i^j + c_i^{j+1}}{(\Delta y)^2} + R_i^j \quad (9)$$

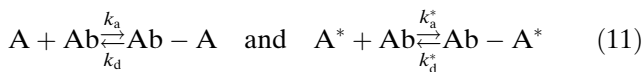
where Δy is the grid cell size in cross-stream direction, and index j ($1 \leq j \leq J-1$) represents the cross-stream location in the grid. J is the number of the grid cells.

Equation 9 can be recast into a more intuitive form in terms of a set of first-order (evolution-typed) ODEs,

$$\dot{c}_i^j(x) = f(c_i^{j-1}(x), c_i^j(x), c_i^{j+1}(x)) \tag{10}$$

where $\dot{c}_i^j(x)$ represents the first-order derivative of c_i^j with respect to x . The reactive source term R_i^j in Eq. 9 is specific to the reaction mechanism. Here we describe R_i^j for two commonly encountered types of biochemical reactions: competitive immunoassays and Michaelis–Menten-type enzyme reactions.

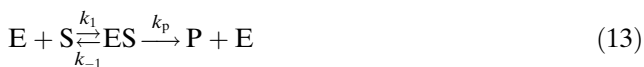
Competitive immunoassays In a competitive immunoassay, the antigen (A) and labeled antigen (A^*) compete for a limited number of binding sites of the antibody (Ab) (Chiem and Harrison 1998; Hatch et al. 2001) to form an antibody–antigen complex ($Ab-A$ or $Ab-A^*$). The reactions are described as



where k_a and k_d are the rate constants for the forward (association) and backward (dissociation) reactions, respectively. The asterisk signifies the quantities associated with the labeled antigen A^* . The source terms arising from the reactions are:

$$\begin{aligned} R_A &= -R_{Ab-A} = -k_a c_A c_{Ab} + k_d c_{Ab-A} \\ R_{A^*} &= -R_{Ab-A^*} = -k_a^* c_{A^*} c_{Ab} + k_d^* c_{Ab-A^*} \\ R_{Ab} &= -k_a c_A c_{Ab} - k_a^* c_{A^*} c_{Ab} + k_d c_{Ab-A} + k_d^* c_{Ab-A^*} \end{aligned} \tag{12}$$

Michaelis–Menten enzyme reactions The mechanism of enzyme-catalyzed reactions involving the enzyme (E), substrate (S), and the product (P) can often be described by (Voet et al. 1999)



where P is the product, ES is the enzyme–substrate complex, k_1 and k_{-1} are the forward and backward rate constants for the formation of ES, and k_p is the kinetic constant for conversion of the enzyme–substrate complex to the product. When the substrate concentration far exceeds that of the enzyme, the rate of product formation can be described by Michaelis–Menten kinetics. Schilling et al. (2002) show that for microfluidic assays that involve non-uniform analyte concentrations across the stream, reactive source terms for enzyme, substrate, and product can be written as (Schilling et al. 2002)

$$R_S = -R_P = -\frac{k_p c_E c_S}{K_m + c_S} \quad \text{and} \quad R_E = 0 \tag{14}$$

where K_m is the Michaelis constant. R_s and R_p can be substituted into Eq. 5 to determine spatial analyte concentration profiles.

3.2 Surface biochemical reaction-based assays

Microfluidic devices currently being developed for drug screening as well as diagnostic applications increasingly involve biochemical assays with surface-immobilized receptors (enzymes, antibodies, etc.). Design of such assays requires an understanding of the balance between reaction kinetics and the rate of convective–diffusive transport to the reaction surface. In this section, we will present models for predicting the transient cross-sectional average concentration of the analyte in non-reactive and reactive components in such systems.

3.2.1 Non-reactive components: channels and junctions

For microchannels that do not involve surface reactions, we also assume that: (1) the channels are sufficiently long (or enhanced mixing is applied) and analyte concentrations are transversely uniform at their outlets. This restricts the model applicability, for example, in a channel where two parallel analyte streams mix solely through lateral diffusion, $Pe_i w/L \ll 1$ needs to be satisfied for model to be valid (2) analyte band broadening due to axial dispersion (Taylor dispersion) is negligible compared with the length of the analyte band (determined by the time for analyte supply). Based on the assumptions, the average analyte concentration within the network is dependent only on flow rate (or electrical current) distribution (Chatterjee and Aluru 2005; Dertinger et al. 2001; Jacobson et al. 1999) and analyte residence time (time delay) in the channel. Thus, it is adequate to capture the cross-sectional average analyte concentration and the time lag (for optimal experimental design).

For the channels, we neglect the transverse diffusion and volumetric reactive terms in Eq. 5. The average analyte concentration at the channel outlet $c_i^{(out)}(t)$ can be treated as a translation of that at the inlet $c_i^{(in)}(t)$ by a time lag t_i (mean analyte residence time in the channel). This yields

$$c_i^{(out)}(t) = c_i^{(in)}(t - t_i) \tag{15}$$

where indices in and out represent the quantities at the inlet and outlet, respectively; $t_i = L/U_i$ is the mean residence time of the i th analyte within the channel.

The merging junction combines two incoming streams respectively with average analyte concentrations $c_i^{(l)}(t)$ and $c_i^{(r)}(t)$. Because of the small flow path lengths associated with the junction, the resulting analyte time lags are neglected. Considering an overall mass balance for the merging junction, the average analyte concentration at the outlet $c_i^{(out)}(t)$ is given by

$$c_i^{(out)}(t) = c_i^{(l)}(t) \cdot s + c_i^{(r)}(t) \cdot (1 - s) \quad (16)$$

where s is the flow rate ratio of the left stream to the total.

For the splitting junction, the average analyte concentrations at the left and right outlets, $c_i^{(l)}(t)$ and $c_i^{(r)}(t)$, are found as

$$c_i^{(l)}(t) = c_i^{(in)}(t) \quad \text{and} \quad c_i^{(r)}(t) = c_i^{(in)}(t) \quad (17)$$

where $c_i^{(in)}(t)$ denotes the average analyte concentration at the channel inlet. Equation 17 shows that average analyte concentrations at the left and right outlet are same as that at the inlet.

3.2.2 Surface reactors

In surface reactors, the analyte flux \tilde{q} at the reaction surface actually induces a non-uniform analyte concentration along the channel depth z . To capture such effects on surface reaction, we employ a two-compartment modeling approach (Myszka et al. 1998). The model divides the reactor into two compartments (Fig. 3), the bulk (outer) compartment and the surface compartment (representing the region very close to the reaction surface). In each compartment, the analyte concentration is treated as spatially uniform but can vary with time, while the effects of the non-uniformity in analyte concentrations and flow velocities along z are characterized by the mass transport coefficient k_M

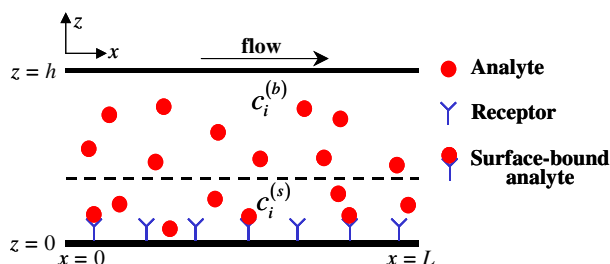


Fig. 3 Schematic of the two-compartment model for surface reaction

between these two compartments (see below). Applying a mass balance to the analyte in the surface compartment, we can obtain (Myszka et al. 1998)

$$0 \approx -\tilde{q}_i + k_M(c_i^{(b)} - c_i^{(s)}) = -\tilde{q}_i + k_M(c_i^{(in)} - c_i^{(s)}) \quad (18)$$

where subscripts b, s, and in denote the quantities in the bulk and surface compartments and the reactor inlet. In Eq. 18, the bulk analyte concentration $c_i^{(b)}$ is set equal to the fresh analyte concentration at the reactor inlet $c_i^{(in)}$ due to the thin concentration boundary layer. The reactive flux \tilde{q}_i at the wall is assumed to be balanced by the mass transfer of the analyte to the surface, leading to a quasi-steady state of $c_i^{(s)}$ (Myszka et al. 1998). k_M is the mass transport coefficient that characterizes the rate of analyte diffusion between the compartments (Lok et al. 1983; Myszka et al. 1998). Likewise, a mass balance to the analyte in the entire reactor yields

$$0 \approx -\tilde{q}_i A_{\text{sur}} + U_i A_c (c_i^{(in)} - c_i^{(out)}) \quad (19)$$

where subscript out denotes the quantities at the reactor outlet; A_{sur} is the surface area of the immobilized receptors; A_c is the channel's cross-sectional area; by the same token, a quasi-steady state assumption is also applied to the entire reactor. In Eq. 19, we also assume that the axial length of the immobilized reactor is small and the associated time lag of the analyte is negligible.

In particular for a reversible analyte–receptor binding reaction, the kinetics can be expressed as



and the reactive analyte flux at the channel wall is given by

$$-\tilde{q}_A = -k_a c_A^{(s)} (\tilde{c}_B^T - \tilde{c}_{AB}) + k_d \tilde{c}_{AB} \quad (21)$$

where A, B, and AB, respectively, are the analyte, receptor binding site, and bound analyte (or called the analyte–receptor complex). \tilde{c}_B^T is the surface concentration (unit: M m) of the total receptor binding sites; $\tilde{c}_B^T - \tilde{c}_{AB}$ denotes the available binding sites. Thus, the average surface concentration of the analyte–receptor complex is given by

$$d\tilde{c}_{AB}/dt = \tilde{q}_A = k_a c_A^{(s)} (\tilde{c}_B^T - \tilde{c}_{AB}) - k_d \tilde{c}_{AB} \quad (22)$$

The approaches used to model different assays and components are summarized in Table 1. For volumetric

Table 1 Modeling approaches used for different assay components

Assay type	Solution variables	Reactor model	Non-reactive components
Volumetric	Cross-stream concentration profiles	Method of lines	Fourier series expansion
Surface	Cross-sectional average concentration	Two-compartment approach	Mass balance

assays, the MOL and Fourier series expansion are, respectively, employed to model cross-stream concentration profiles in reactors (Sect. 3.1.2) and non-reactive components (Sect. 3.1.1), e.g., channels, mergers, and splitters. For surface assays, the two-compartment approach and mass balance are used to evaluate the cross-sectional average concentration in reactor (Sect. 3.2.2) and non-reactive components (Sect. 3.2.1).

4 Solution methodology

As described in Sect. 2, the LoC system is represented as a network of microfluidic components. The governing equations for pressure-driven fluid flow (Eq. 1) and electroosmotic flow (Eq. 3) are then solved in the network. The pressure and velocity fields are coupled using an implicit pressure-based scheme—SIMPLE (semi-implicit method for pressure-linked equations) (Patankar 1980). The distribution of electric potential and currents is computed using Kirchhoff’s law (Wang et al. 2006b). In both cases, the software library SuperLU (<http://crd.lbl.gov/~xiaoye/SuperLU/>) is used for matrix inversion (to solve the resulting system of linear equations). SuperLU is a general-purpose library for direct solution of large, sparse, non-symmetric systems of linear equations. The details of the network formulation and solution methodology are presented elsewhere (Bedekar et al. 2006). The flow field calculated is then used to solve the governing equations for analyte transport. Since the analyte transport and biochemical reactions occurring in different components are described by disparate modeling approaches (e.g., the numerical MOL model for the volumetric reactor and Fourier series-based solution for the analyte mixing in volumetric reactions-based assays, etc.), proper exchange of information between components is critical. For volumetric reactions-based assays, Fourier cosine series coefficients $\{d_{i,n}^{(g)}\}^k$ of the cross-stream analyte concentration profile are propagated in the network, which at the volumetric reactor are converted back and forth to discrete concentration

profiles c_i^j (note that c_i^j is needed in Eq. 9) using the conversion functions

$$c_i^j = \sum_{n=0}^{\infty} d_{i,n}^{(in)} \cos\left(n\pi \frac{j}{J}\right) \tag{23}$$

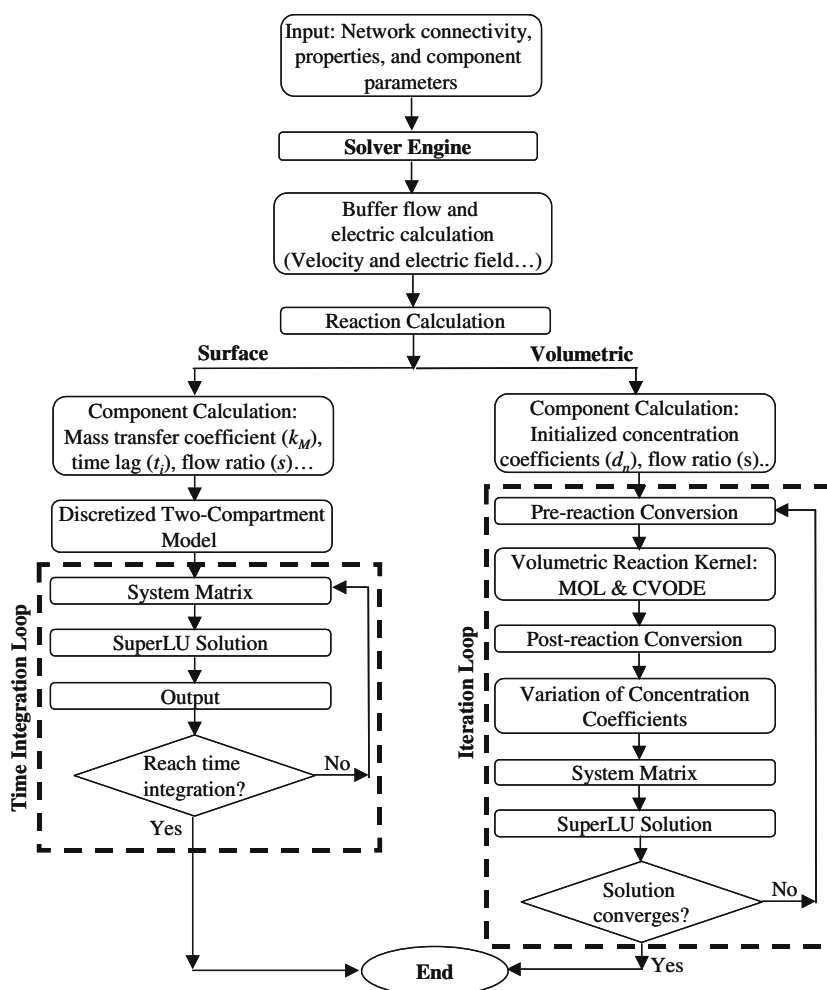
$$d_{i,n}^{(out)} = a_n \sum_{j=0}^J \frac{c_i^j \cos\left(n\pi \frac{j}{J}\right)}{J} \tag{24}$$

where $a_n = 1$ for $n = 0$ and $a_n = 2$ for $n \neq 0$ (from orthogonality of Fourier eigenfunctions), index k is for the k th component in the network and g can be in or out (indicating the inlet or outlet, respectively). Equations 23 and 24 allow us to restrict the use of the MOL-based numerical ODE models (which are computationally expensive) to volumetric reactors only, rather than for the entire network. This makes it possible to achieve rapid solutions without appreciably compromising the accuracy. For numerical integration of ODEs (Eq. 9), we use the software library CVODE (<http://www.llnl.gov/CASC/sundials/>). When surface reactions-based assays are considered, the average analyte concentration $\{c_i^{(g)}\}^k$ is employed in the network representation. Parameter values of analyte transport at the component’s outlet are calculated based on the corresponding values at the inlet and contributions from the component itself using Eqs. 6–22. This information is then assigned as the input to the next component downstream (i.e., $\{d_{i,n}^{(in)}\}^{k+1} = \{d_{i,n}^{(out)}\}^k$ and $\{c_i^{(in)}\}^{k+1} = \{c_i^{(out)}\}^k$).

The current implementation allows for a virtually arbitrary number of different analytes coexisting in the buffer subjected to the limit of computational resources. For the simulation of the volumetric biochemical assays, 40 Fourier terms ($n = 0, 1, \dots, 39$), and eighty grid cells along the width ($J = 80$) were found to yield sufficient accuracy in most LoC applications.

Figure 4 summarizes the flow chart of our system-level simulation of LoC systems. Simulation information (such as the connectivity between components, analyte and component parameters) is read by the solver and used to solve the flow and electric field (Bedekar et al. 2006). The solver then initiates the solution of the governing equations for analyte transport (note that the electrical and flow calculations are decoupled from analyte transport). For surface reactions, a calculation is first looped on each component to obtain process-related parameters, such as mass transfer coefficients in reactors and flow ratios s at junctions. These parameters are substituted into the discretized two-compartment model that is then

Fig. 4 Flow chart of the system-level simulation of biochemical assays in lab-on-a-chip devices



assembled into the system matrix along with the information of flow and component connectivity. The matrix is efficiently solved using SuperLU for $\{c_i^{(g)}\}^k$ in the network. Matrix assembly and solving steps proceed iteratively until the user-defined integration time is reached. This process also applies to the volumetric reaction with the major difference that the CVODE is used to evaluate the discrete concentration profiles at reactors (Sect. 3.1.2) and the Fourier coefficients $\{d_{i,n}^{(g)}\}^k$ of the sample concentration are captured at component terminals. When multiple volumetric reactors simultaneously coexist in an assay, the analyte concentration profile input to the reactor downstream depends on the output from the upstream reactor; hence, iterations are also needed.

5 Results and discussion

In this section, the system-level model will be applied to practical LoC assays, including volumetric com-

petitive immunoassay, Michaelis–Menten enzyme reactions, and the reversible analyte–receptor binding reactions. Validation of the models by comparison with experimental data extracted from the literature and high-fidelity numerical analysis are also presented. Numerical analysis is performed with the commercial finite volume-based simulation software CFD-ACE+ (ESI-CFD, Inc.). The computational domain is meshed by a block-structured grid using the preprocessor available within CFD-ACE+. The software solves the 3D Navier–Stokes equations for incompressible fluid flow and convection–diffusion equation with reaction for the buffer flow velocity and analyte concentration, respectively, in the microfluidic device. The CFD-ACE+ solver uses the SIMPLEC algorithm for pressure–velocity coupling. An upwind scheme is used for discretization of the velocity fields, while a second-order scheme is used for analyte distribution. The linearized algebraic equations are solved using an algebraic multi-grid (AMG) iterative method for accelerated convergence.

5.1 Competitive immunoassay

To examine the accuracy and efficiency of the models (as well as the integration of the SuperLU and CVODE numerical libraries to our simulation engine), we first compare our modeling results with CFD-ACE+ and experimental data for a competitive immunoassay chip with a Y-channel design (Fig. 5).

Premixed analytes comprising antigen A and labeled antigen A^* (in white) flow into the main channel where they compete for a limited number of binding sites of antibody Ab (in black) from the left branch (Fig. 5a). Figure 5b shows the comparison of system-level simulation results, CFD-ACE+ analysis, and extracted experimental data (Hatch et al. 2001) on the normalized fluorescence intensity along the channel width for different inlet antigen concentrations (c_A). The fluorescence intensity measured in experiments is linearly proportional to the total concentration of A^* and $Ab-A^*$. Excellent agreement between experimental and simulation results with an average relative error less than 5% has been obtained. The concentration peak near the channel centerline is caused by an accumulation of complex $Ab-A^*$ and exhibits a higher value when the relative A^* concentration is larger (e.g., $c_A = 0$). As c_A increases, more Ab binding sites tend to be occupied by the unlabeled antigen A, leading to negligible binding of A^* . Thus, a monotonic sigmoid distribution of the fluorescence intensity resulting from pure molecular diffusion of A^* is observed.

The accuracy of the CVODE library is also verified by comparing the same results from (Hatch et al. 2001) using Matlab ODE solver. The difference is indistinguishable. In addition, our system-level simulation achieves considerable speedup over the full numerical

analysis using CFD-ACE+. On an MS-Windows workstation with an AMD Athlon CPU (2 GHz, 1 GB RAM), a single system-level simulation in Fig. 5 takes ~1.4 s, while the 3D numerical model uses about 700 s, yielding about 500-fold speedup.

5.2 Michaelis–Menten-type enzyme assay

Next we apply the system-level model to the integrated LoC system for cell lysis and detection shown in Fig. 1. *Escherichia coli* cells and lysis agent flow side by side in the long lysis channel (L3) to release the intracellular contents. The small intracellular molecules, such as enzyme β -galactosidase (β -gal), diffuse faster to the right half of the channel. Molecules, such as DNA and the lysed cell residue tend to remain in the left half channel due to their relatively large size and small diffusivity. At the splitting junction (T2), the flow stream is split and a fraction of the β -gal is extracted and transported via merging junction (T3) to the volumetric reaction channel (VR1), where it reacts with the fluorogenic substrate β -D-galactopyranoside (RBG) for a Michaelis–Menten-type enzyme reaction. Figure 6 compares the cross-stream concentration profiles of enzyme β -gal from the system-level simulation with those from CFD-ACE+ analysis (simulation parameters are given in Appendix B) at different locations. The diffusion of β -gal into the lysis stream at the end of the lysis channel (L3) is observed at station 1. Immediately downstream of the merging junction T3 (station 2) an abrupt concentration gradient of enzyme β -gal is found at its interface to the substrate (RBG) stream. The gradient gradually smears out along the detection channel (station 3). Excellent agreement (relative error < 6.3%) between system simulation and

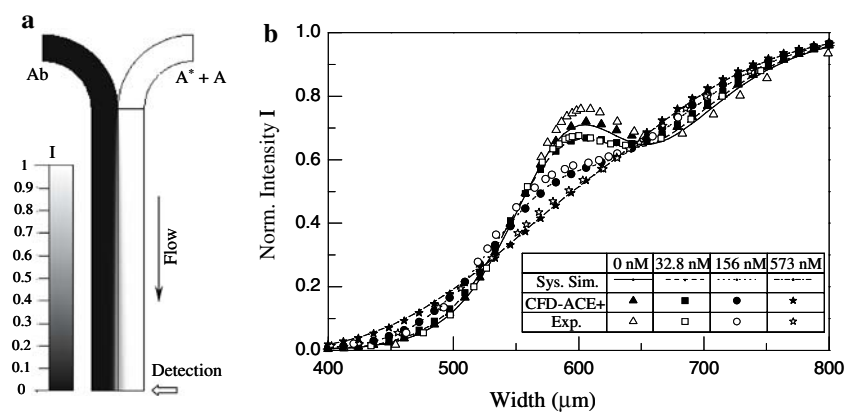
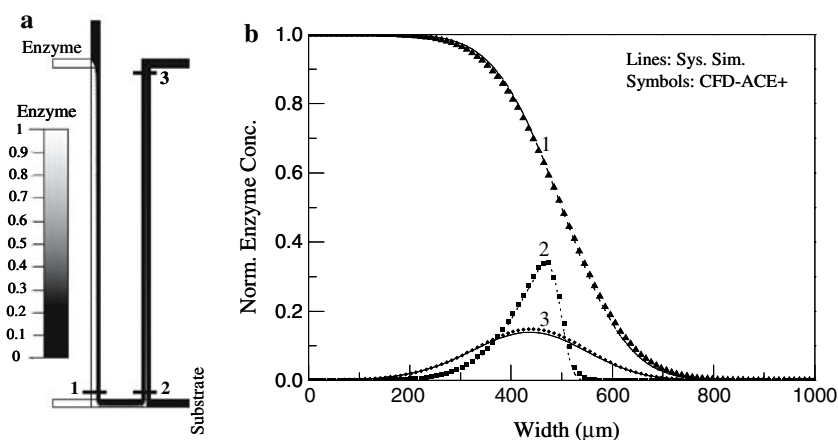


Fig. 5 **a** Schematic of the Y-type competitive immunoassay and the contour plot of the normalized fluorescence intensity (I) from CFD-ACE+. **b** Comparison between system-level simulation (Sys.Sim.) results, high-fidelity numerical analysis (CFD-ACE+),

and experimental data [exp., extracted from Hatch et al. (2001)] in terms of normalized fluorescence intensity along the channel width

Fig. 6 Comparison between system-level simulation and CFD-ACE+ results on cross-stream concentration profiles of β -gal in the chip in Fig. 1 at three locations (see numerical plot on the left)



CFD-ACE+ results and tremendous speedup (10,000-fold) has been achieved. It should be pointed out that the concentration profile at the inlet of the reaction channel (station 2) is particularly important for determining the rate constants of the enzyme reaction, which previously needed time-consuming numerical analysis (Schilling et al. 2002; Wang et al. 2006a).

Figure 7 shows the comparison between the system-level simulation results and experimental data on the cross-stream concentration profile of Resorufin extracted at 1 and 2.7 mm downstream of the detection/reaction channel inlet. We use the same two-step simulation procedure formulated in (Schilling et al. 2002) to take into account the different viscosities of sample and lysis agent streams. There is good agreement between simulation and experimental data. Since the enzyme reaction is fast relative to the cross-stream diffusion, the reaction product (Resorufin) accumulates at the interface between the two streams leading to a concentration peak. With constant inputs of the substrate concentration and the flow rates, this profile

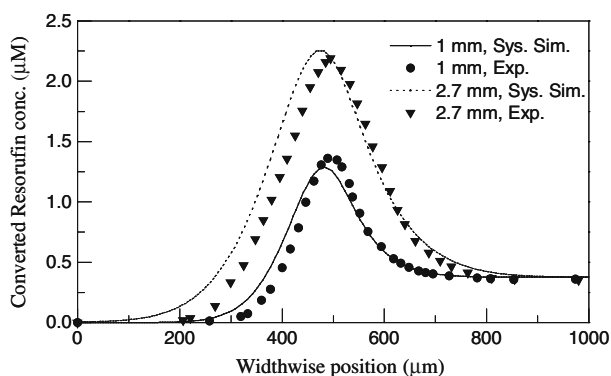


Fig. 7 Comparison of Resorufin (enzyme reaction product) concentration profiles for system-level simulations and experimental data. The concentration profiles are extracted at 1 and 2.7 mm downstream from the inlet of the detection/reaction channel (see Fig. 1)

is uniquely determined by the enzyme concentration alone, and hence, can be used for measurement of cell concentrations.

Figure 8 shows another automated enzyme chip, which is driven by electrokinetic flow (Hadd et al. 1997). The fluorogenic substrate (β -gal) from reservoir 1 (Fig. 8a) first merges with the dilution buffer from reservoir 2 at the MIX junction. The diluted substrate then flows into the cross intersection (RXN junction) where it is sandwiched by the enzyme and buffer streams from both sides. In the reaction channel, the Michaelis–Menten reaction occurs between the substrate and enzyme accompanied by the molecular diffusion-based mixing to produce the fluorescent product Resorufin. By modulating electrical potentials at the substrate and buffer reservoirs, different flow rate ratios, dilution ratios, substrate concentrations, and the reaction rates can be attained in experiments, from which constants K_m and k_p (Eq. 14) can be extracted. In our system-level simulation, the enzyme chip is decomposed into a set of reservoirs, mixing channels, merging junctions, and volumetric reaction channel (Fig. 8b). Note that the cross RXN junction is treated as a cascade concatenation of two merging junctions.

Figure 9 shows the cross-sectional area-averaged resorufin concentration calculated 20 mm (Hadd et al. 1997) downstream from the RXN junction as a function of substrate and enzyme concentrations at the reservoir inlet. Results from system-level simulations and CFD-ACE+ analysis are compared (simulation parameters are given in Appendix B). From Fig. 9, we see that an increase in substrate and enzyme concentrations results in a growth in resorufin generation. However, at a constant enzyme concentration the growth of the resorufin versus substrate concentration is nonlinear and becomes slower at high substrate (RBG) concentrations, which agrees with prediction in Eq. 14. Excellent agreement between the system sim-

Fig. 8 **a** Schematic of the automated enzyme assay chip. The insets show the concentration contours of the substrate (RBG) and product (β -galactosidase) from CFD-ACE+. **b** Network representation for system-level simulation

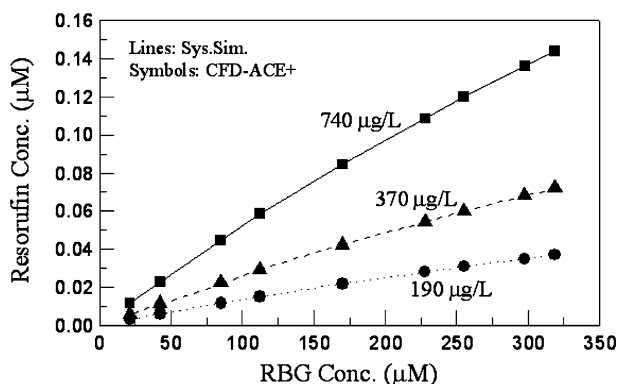
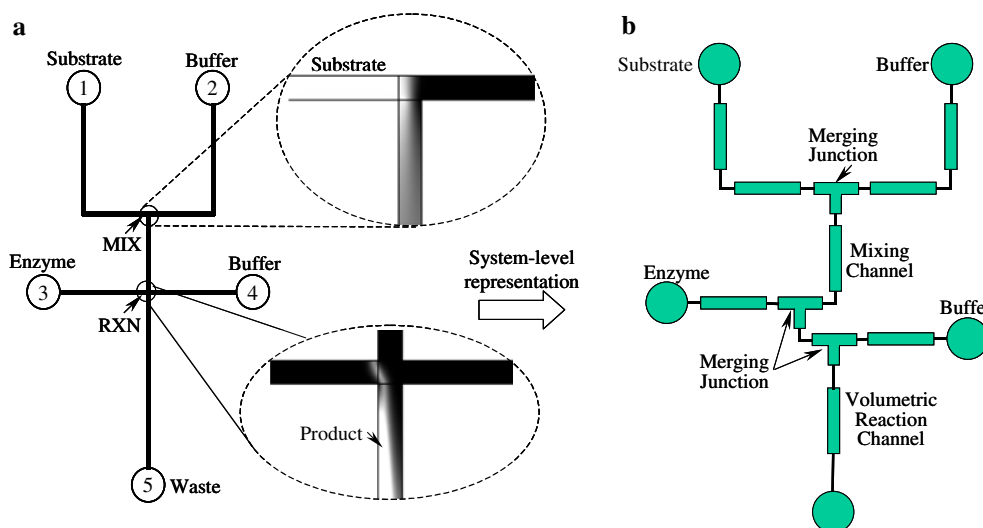


Fig. 9 The concentration of the enzyme reaction product (resorufin) versus substrate (RBG) and enzyme (β -gal) concentrations. Three enzyme concentrations {190, 370, and 740} $\mu\text{g/L}$ are selected as in Hadd et al. (1997)

ulation and CFD-ACE+ analysis has been achieved with the average relative error less than 1%.

5.3 Surface-immobilized reversible binding assay

Figure 10 shows the comparison between the transient system-level simulation and experimental data from the BIACORE™ kinetics analyzer (BIACORE International, Uppsala, Sweden) for the binding of acetazolamide (analyte) to surface-immobilized anhydrase-II (receptor) (Wang et al. 2006a). The experimental data show the transient response of the reflective unit (RU), which is linearly proportional to the surface concentration of the bound acetazolamide in surface plasmon resonance (SPR) measurements. Other simulation parameters are given in the Appendix B. The analyte supply is initiated at $t = 0$ s and terminated at 90 s. We can see that the bound acetazolamide

increases with time but at a decreasing rate due to a reduction in available anhydrase-II binding sites as the reaction proceeds, then levels off and reaches a steady state. After analyte supply is cut off, the bound analyte disassociates and restores to the initial state. As inlet concentration of acetazolamide increases, reaction rate grows dramatically, leading to a faster approach to the equilibrium and a higher equilibrium concentration. These transient response curves at different flow-in analyte concentration have been practically used to extract the kinetic and rate constants.

To achieve high-throughput analysis, reaction and concentration array networks can be combined (Bernard et al. 2001; Jiang et al. 2003) as depicted in Fig. 11. The concentration array network continuously splits and recombines the analyte and buffer streams, eventually resulting in a linear concentration array at the inlets of channels A–E. Stripes presenting different immobilized receptors intersect with channels A–E. Thus, the device enables simultaneous analysis of multiple candidate receptors at a wide range of analyte concentration, and is well suited to study of binding specificity in clinical diagnostics and drug discovery (Bernard et al. 2001). In our approach, the concentration array network is disassembled into a set of channels, merging and splitting junctions as described in Sect. 3.2. Channels A–E, each containing four surface reactors, is decomposed into a series of alternately linked reactors and channels. Figure 12 illustrates the transient response of the surface concentration of the analyte–receptor complex in reactors along channel A (A_1 – A_4) and along strip 1 (A_1 – D_1). An analyte of 50 nM is supplied at the inlet reservoir, yielding a linear concentration array {50, 37.5, 25, 12.5, 0} nM at the

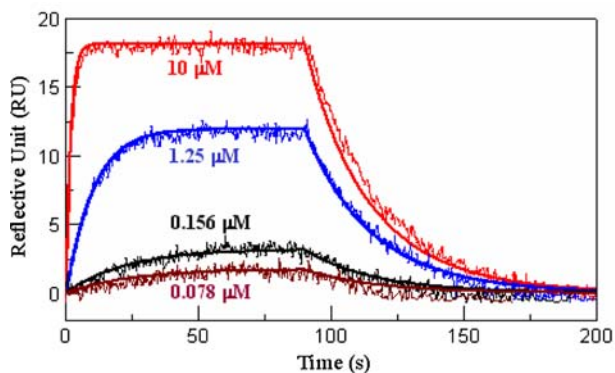


Fig. 10 Comparison between system simulation (*smooth curves*) and BIACORE data (*fluctuating curves*) for the binding of acetazolamide to surfaced immobilized anhydrase-II at different inlet acetazolamide concentrations

inlets of channels A–E. Receptors with increasing binding affinity to the analyte, $k_a = \{4 \times 10^4, 4 \times 10^5, 4 \times 10^6, 4 \times 10^7\} \text{ M}^{-1} \text{ s}^{-1}$ (k_d remains 0.02 s^{-1}), are respectively immobilized on strips 1–4. Figure 12a illustrates the transient response in reactors along strip 1 that involve different flow-in analyte concentrations. It exhibits the similar binding behavior as the experimental data in Fig. 10. Figure 12b shows the response of the surface reactors along channel A. As the forward binding constant k_a increases, the reaction rate raises dramatically, leading to a faster arrival to the equilibrium state and a higher equilibrium value. It is interesting to note that at extremely high k_a (e.g., for A_4 , $k_a = 4 \times 10^7 \text{ M}^{-1} \text{ s}^{-1}$), the analyte–receptor concentration ascends almost linearly at the beginning and the reaction is transport limited.

It should be pointed out that all curves presented in Fig. 12 are generated by a single simulation, which is completed within 40 s and contains more than 120 components and 20 surface reactors. This is the first time that a system-level simulation is used for evaluating performance of multiple surface-immobilized reactors in complex microfluidic networks and high-throughput assays.

6 Conclusions

We have presented an efficient and accurate system-level modeling and simulation approach for LoC design. Integrated LoCs are decomposed into a collection of components with relatively simple geometries and specific functionalities. Numerical ODE models for biochemical reactions in reactors and analytical models for fluid flow, electric field, and sample transport in other microfluidic components (e.g., channels and junctions) are also developed. The models demonstrate substantial computational speedup without appreciably compromising accuracy, and are therefore well suited for optimal design of microchips as well as determination of kinetic constants (or other process-related parameters) from experimental measurements—a process that typically involve a large number of simulation iterations.

We also present approaches to seamlessly link the component models developed by disparate approaches for a system-level simulation. The communication between adjacent components is enabled through a proper choice of the parameters at component inter-

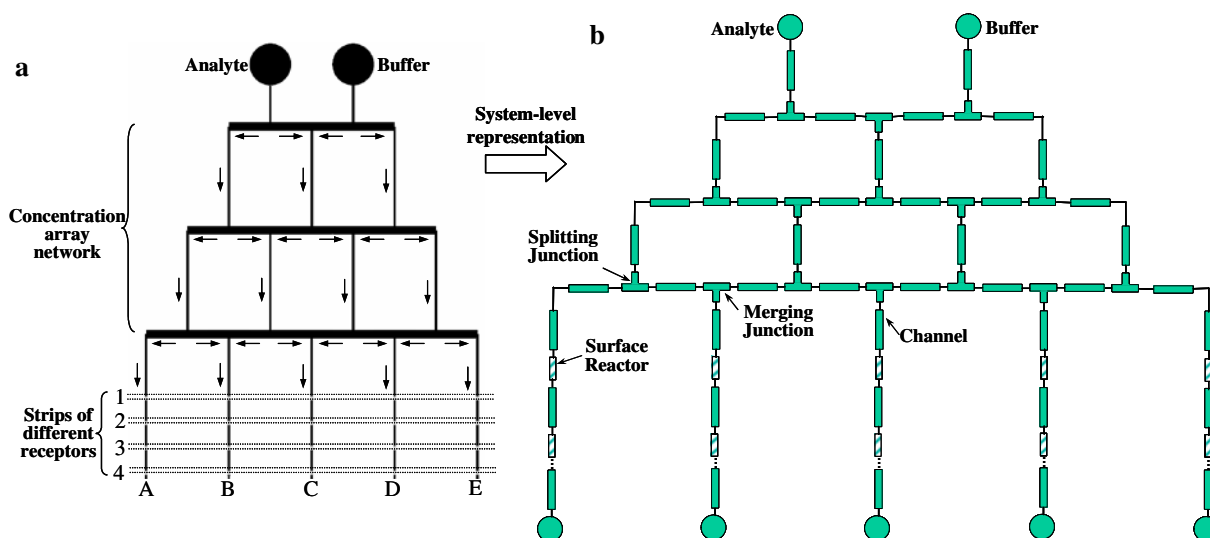


Fig. 11 **a** Sketch of a high-throughput assay for kinetic analysis, consisting of two subsystems: a concentration array network and a surface binding reaction array network. **b** Its schematic for system-level simulation

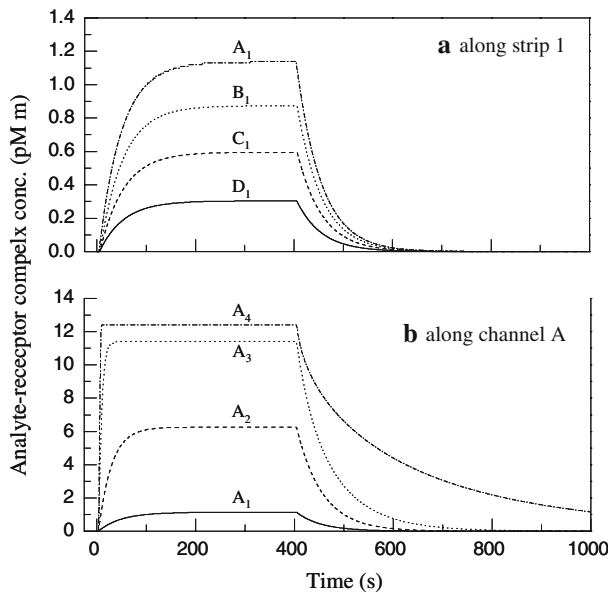


Fig. 12 Transient response of the surface concentration of the analyte–receptor complex in surface bioreactors. **a** Along channel A; **b** along line *l*

faces. Specifically, Fourier cosine series coefficients of cross-stream analyte concentration profiles $\{d_n\}$ and cross-sectional average analyte concentration c are, respectively, used in the network representation of volumetric and surface reaction-based LoC assays. Pre-reaction and post-reaction conversion algorithms are proposed within volumetric reactors to convert the discrete analyte concentration profile into Fourier series back and forth. This restricts the use of numerical model only for reactors and ensures fast simulation speed. These models have been integrated into an efficient simulation engine for system-level simulation of the entire chip and allow for rapid iterative design of LoCs.

The system-level simulations have been validated against high-fidelity numerical analysis and experimental data, and applied to evaluating system performance of practical LoCs including competitive immunoassay, pressure-driven and electrokinetic Michaelis–Menten-type enzyme assays, and surface binding reaction. It has been shown that the models are

able to accurately describe the overall effects of the system topologies and design protocols on chip performance, and interactions among components. Tremendous speedup (100–10,000-fold depending on assays) over high-fidelity CFD analysis has been achieved, while still maintaining adequate accuracy (<10% error relative to numerical analysis). Therefore, our modeling and simulation efforts represent a significant contribution to addressing the need for efficient and accurate modeling and simulation tools for optimal design of integrated LoC assays. On incorporating optimization algorithms, the present effort can be readily extended to chip layout optimization and kinetics analysis.

In the future, more diverse reaction modules, such as surface-immobilized enzymatic assays and other multi-step reaction mechanisms, can be built to further extend the current effort. In addition, to achieve a fully integrated and multi-functional total analysis LoC system, a generalized approach that integrates these models to the previously developed electrophoresis models needs to be proposed (Bedekar et al. 2006).

Acknowledgments This research is sponsored by the National Aeronautics and Space Administration (Contract No. NNC04CA05C) and an internal R&D grant from CFD Research Corporation. The authors would like to thank Drs. Jerry W. Jenkins and David G. Myszka for providing and interpreting the BIACORE data and simulation parameters.

7 Appendix A: Component models for mergers and splitters (Sect. 3.1.1)

The merger is another component commonly used in LoC assays. In a merger two incoming streams with certain analyte concentration profiles are combined and emerge as a single merged stream. Denote $d_{i,m}^{(l)}$ and $d_{i,m}^{(r)}$ ($m = 0, 1, 2, \dots$) the Fourier coefficients of concentration profiles of the i th analyte at the left and right inlets, respectively. Then Fourier coefficients $d_{i,n}^{(out)}$ ($n = 0, 1, 2, \dots$) at the merger outlet can be obtained as (Wang et al. 2005a, 2006b),

$$d_{i,n}^{(out)} = \begin{cases} d_{i,0}^{(l)}s + d_{i,0}^{(r)}(1 - s), & \text{if } n = 0 \\ s \sum_{m=0}^{\infty, \text{if } m \neq ns} d_{i,m}^{(l)} \frac{f_1 \sin(f_2) + f_2 \sin(f_1)}{f_1 f_2} + s \sum_{m=0}^{\infty, \text{if } m = ns} d_{i,m}^{(l)} + (1 - s) \sum_{m=0}^{\infty, \text{if } m = n(1-s)} (-1)^{n-m} d_{i,m}^{(r)} + 2(-1)^n (1 - s) \sum_{m=0}^{\infty, \text{if } m \neq n(1-s)} d_{i,m}^{(r)} \left(\frac{\cos(F_2/2) \sin(F_1/2)}{F_1} + \frac{\cos(F_1/2) \sin(F_2/2)}{F_2} \right), & \text{if } n \geq 1 \end{cases} \quad (A1)$$

where $s = q_l/(q_l + q_r)$ is the flow ratio, the normalized flow rate of the left-side stream, and also the normalized position of the interface between the incoming streams. In Eq. A1, $f_1 = (m - ns)\pi$, $f_2 = (m + ns)\pi$, $F_1 = (m + n - ns)\pi$, and $F_2 = (m - n + ns)\pi$. Since the analyte concentration profiles from the inlets are scaled down at the outlet, the Fourier series components at the inlet are not orthogonal to those at the outlet. Therefore, different indices m and n are used at the inlets and outlet, respectively.

The splitter splits a single incoming stream into two that emerge at the left- and right-side outlets. Let $d_{i,m}^{(in)}$ ($m = 0, 1, 2, \dots$) be the Fourier coefficients of concentration profile of the i th analyte at the inlet. Its Fourier coefficients at the left and right outlets are given by

$$d_{i,n}^{(l)} = \begin{cases} d_{i,0}^{(in)} + \sum_{m=1}^{\infty} d_{i,m}^{(in)} \sin(\phi_1) / \phi_1 & \text{if } n = 0 \\ 2 \sum_{m=0}^{\infty, \text{ if } m \neq n/s} d_{i,m}^{(in)} (-1)^{n+1} \phi_1 \sin(\phi_1) / f_1 f_2 + \sum_{m=0}^{\infty, \text{ if } m=n/s} d_{i,m}^{(in)} & \text{if } n \geq 1 \end{cases} \quad (\text{A2})$$

and

$$d_{i,n}^{(r)} = \begin{cases} d_{i,0}^{(in)} - \sum_{m=1}^{\infty} d_{i,m}^{(in)} \sin(\phi_1) / \phi_2 & \text{if } n = 0 \\ 2 \sum_{m=0}^{\infty, \text{ if } m \neq n/(1-s)} d_{i,m}^{(in)} \phi_2 \sin(\phi_1) / F_1 F_2 + \sum_{m=0}^{\infty, \text{ if } m=n/(1-s)} (-1)^{m-n} d_{i,m}^{(in)} & \text{if } n \geq 1 \end{cases} \quad (\text{A3})$$

where $f_1 = (n - ms)\pi$, $f_2 = (n + ms)\pi$, $F_1 = (n + m - ms)\pi$, $F_2 = (n - m + ms)\pi$, $\phi_1 = ms\pi$, and $\phi_2 = m(1 - s)\pi$. Here, $s = q_l/(q_l + q_r)$ is the splitting flow ratio, as well as the normalized interface position between the two split streams. By the same reason, different indices m and n are used at the inlet and outlets.

8 Appendix B: Extraction of experimental and numerical data from the literature

8.1 Parameters for the competitive immunoassay (Sect. 5.1)

We use data from competitive immunoassay experiments in a Y-sensor reported by Hatch et al. (2001) to validate the implementation of CVODE numerical package and SuperLU matrix solver in our system-level simulation framework. Same parameters as the experiments are used: $k_a = k_a^* = 4 \times 10^{-6} \text{ M}^{-1} \text{ s}^{-1}$, $k_d = k_d^* = 1 \times 10^{-4} \text{ s}^{-1}$, $D_A = 5.8 \times 10^{-10} \text{ m}^2/\text{s}$, $D_{A^*} = 3.2 \times 10^{-10} \text{ m}^2/\text{s}$, $D_{Ab} = D_{Ab-A} = D_{Ab-A^*} = 4.3 \times 10^{-11} \text{ m}^2/\text{s}$. c_{Ab} and c_{A^*} in reservoirs are hold constant at 74

and 19 nM, respectively. The detection is made at 6.4 mm downstream of the merging junction, yielding a residence time of 18.5 s for the analytes and antibody. In the numerical CFD-ACE+ model, the depth and width of the channel are, respectively, resolved with 10 and 120 cells, yielding 83,000 cells for the entire volume.

8.2 Parameters for the Michaelis–Menten enzyme reaction (Sect. 5.2)

We use data from two enzymatic assays, respectively, in pressure-driven (Schilling et al. 2002) (see Fig. 1) and electrokinetic (Hadd et al. 1997) flow. For the former, parameters used in the system simulations are: $K_m = 538 \text{ } \mu\text{M}$, $k_p = 70 \text{ s}^{-1}$, $D_E = 2.7 \times 10^{-11} \text{ m}^2/\text{s}$, $D_S =$

$4.3 \times 10^{-10} \text{ m}^2/\text{s}$, $D_P = 6.6 \times 10^{-10} \text{ m}^2/\text{s}$ as reported. The enzyme concentration c_E specified at the cell inlet in the system simulation and CFD-ACE+ analysis is $0.4714 \text{ } \mu\text{M}$, yielding a maximum enzyme concentration of $0.165 \text{ } \mu\text{M}$ at station 3 as discussed in (Schilling et al. 2002). The data reflect the fluorescence intensity contributed by both the product (Resorufin) and substrate (RBG). The substrate concentration c_S at the substrate inlet is $50 \text{ } \mu\text{M}$. In the numerical CFD-ACE+ model, the depth and width of the channel are, respectively, resolved with 8 and 60 cells, yielding 440,000 cells for the entire volume. For the electrokinetic assay, from the electrical resistance of each channel, we calculate each channel length in Fig. 8a. The channels linking to reservoirs 1, 2, 3, and 4 are, respectively, 2.064, 2.566, 0.804, and 0.684 cm. Mixing and reaction channels are 0.188 and 2.34 cm long, respectively. Electrokinetic mobility is $3.47 \times 10^{-8} \text{ m}^2/(\text{Vs})$, yielding a flow rate of 14 nL/s (Hadd et al. 1997). Enzyme concentrations of {190, 370, and 740} $\mu\text{g/L}$ identical to the experiments are used, which are converted to {0.352, 0.685, 1.37} nM in system-level simulation and CFD-ACE+ using information in (Schilling et al. 2002). As feed channels

do not affect analyte mixing and reaction downstream, CFD-ACE+ simulations are only performed on the mixing and reaction channels with the voltage at their inlet set to a value calculated from the system-level model. In electrokinetic flow, the analyte concentrations are assumed to be independent of the coordinate along the channel depth (Ermakov et al. 1998). We hence model the device in 2D domain and the channel width is discretized into 40 segments, giving a total of 66,000 cells. Our CFD-ACE+ analysis (not shown) indicates that the concentrations of the enzyme, substrate, and product are completely uniform along the channel width at the detection spot. Therefore, the resorufin concentration in the vertical axis of Fig. 9 is proportional to the total amount of the resorufin produced (Sect. 5.2).

8.3 Parameters for the surface binding assay (Sect. 5.3)

The BIACORE data are provided by Dr. Jerry W. Jenkins at CFD Research Corporation and is from his private communication with Dr. David G. Myszka at the University of Utah. The reaction channel is 500 μm long and 50 μm wide with an effective binding length of 1.6 mm. The flow rate is 0.785 $\mu\text{L/s}$. Through a global analysis of the BIACORE data using CFD-ACE+ as the iterative subroutine, we find: $k_a = 57,085 \text{ M}^{-1}\text{s}^{-1}$, $k_d = 0.0455 \text{ s}^{-1}$, and $P = 3,215$, where P is the initial RU induced by the blank receptor (anhydrase-II). Anhydrase-II has a molecular weight (MW) of 33,000 g/mol and a RU unit corresponds to 10^{-10} g/cm^2 , which yields the receptor surface concentration of $9.742 \times 10^{-11} \text{ M m}$. Analyte (acetazolamide) has a MW of 201 g/mol.

References

- Ajdari A (2004) Steady flows in networks of microfluidic channels: building on the analogy with electrical circuits. *C R Phys* 5(5):539–546
- Aurouz PA, Lossifidis D, Reyes DR, Manz A (2002) Micro total analysis systems. 2. Analytical standard operations and applications. *Anal Chem* 74(12):2637–2652
- Bedekar AS, Wang Y, Krishnamoorthy S, Siddhaye SS, Sundaram S (2006) System-level simulation of flow-induced dispersion in lab-on-a-chip systems. *IEEE Trans Comput Aided Des Integr Circuit Syst* 25(2):294–304
- Bernard A, Michel B, Delamarche E (2001) Micromosaic immunoassays. *Anal Chem* 73(1):8–12
- Bothe D, Sternich C, Warnecke HJ (2006) Fluid mixing in a T-shaped micro-mixer. *Chem Eng Sci* 61(9):2950–2958
- Chatterjee AN, Aluru NR (2005) Combined circuit/device modeling and simulation of integrated microfluidic systems. *J Microelectromech Syst* 14(1):81–95
- Chiem NH, Harrison DJ (1998) Microchip systems for immunoassay: an integrated immunoreactor with electrophoretic separation for serum theophylline determination. *Clin Chem* 44(3):591–598
- Coelho CP, Desai SD, Freeman D, White J (2005) A robust approach for estimating diffusion constants from concentration data in microchannel mixers. In: Proceedings of 2005 NSTI nanotechnology conference and trade show (Nanotech 2004), Anaheim, CA, pp 549–552
- Cummings EB, Griffiths SK, Nilson RH, Paul PH (2000) Conditions for similitude between the fluid velocity and electric field in electroosmotic flow. *Anal Chem* 72(11):2526–2532
- Dertinger SKW, Chiu DT, Jeon NL, Whitesides GM (2001) Generation of gradients having complex shapes using microfluidic networks. *Anal Chem* 73(6):1240–1246
- Ermakov SV, Jacobson SC, Ramsey JM (1998) Computer simulations of electrokinetic transport in microfabricated channel structures. *Anal Chem* 70(21):4494–4504
- Hadd AG, Raymond DE, Halliwell JW, Jacobson SC, Ramsey JM (1997) Microchip device for performing enzyme assays. *Anal Chem* 69(17):3407–3412
- Hatch A, Kamholz AE, Hawkins KR, Munson MS, Schilling EA, Weigl BH, Yager P (2001) A rapid diffusion immunoassay in a T-sensor. *Nat Biotechnol* 19(5):461–465
- Holden MA, Kumar S, Castellana ET, Beskok A, Cremer PS (2003) Generating fixed concentration arrays in a microfluidic device. *Sensors Actuators B Chem* 92(1, 2):199–207
- Jacobson SC, McKnight TE, Ramsey JM (1999) Microfluidic devices for electrokinetically driven parallel and serial mixing. *Anal Chem* 71(20):4455–4459
- Jiang XY, Ng JMK, Stroock AD, Dertinger SKW, Whitesides GM (2003) A miniaturized, parallel, serially diluted immunoassay for analyzing multiple antigens. *J Am Chem Soc* 125(18):5294–5295
- Kamholz AE, Weigl BH, Finlayson BA, Yager P (1999) Quantitative analysis of molecular interaction in a microfluidic channel: the T-sensor. *Anal Chem* 71(23):5340–5347
- Lok BK, Cheng YL, Robertson CR (1983) Protein adsorption on crosslinked polydimethylsiloxane using total internal-reflection fluorescence. *J Colloid Interface Sci* 91(1):104–116
- Myszka DG, He X, Dembo M, Morton TA, Goldstein B (1998) Extending the range of rate constants available from BIACORE: Interpreting mass transport-influenced binding data. *Biophys J* 75(2):583–594
- Patankar SV (1980) Numerical heat transfer and fluid flow. Hemisphere Publishing Corporation McGraw-Hill, Washington New York
- Reyes DR, Lossifidis D, Aurouz P-A, Manz A (2002) Micro total analysis systems. 1. Introduction, theory, and technology. *Anal Chem* 74:2623–2636
- Schilling EA, Kamholz AE, Yager P (2002) Cell lysis and protein extraction in a microfluidic device with detection by a fluorogenic enzyme assay. *Anal Chem* 74(8):1798–1804
- Voet D, Voet JG, Pratt CA (1999) Fundamentals of biochemistry. Wiley, New York
- Wang Y, Lin Q, Mukherjee T (2005a) A model for laminar diffusion-based complex electrokinetic passive micromixers. *Lab Chip* 5(8):877–887
- Wang Y, Magargle RM, Lin Q, Hoburg JF, Mukherjee T (2005b) System-oriented modeling and simulation of biofluidic lab-on-a-chip. In: Proceedings of the 13th international conference on solid-state sensors and actuators, Seoul, Korea, pp 1280–1283
- Wang Y, Bedekar AS, Krishnamoorthy S, Siddhaye SS, Sundaram S (2006a) Mixed-methodology-based system-level sim-

- ulation of biochemical assays in integrated microfluidic systems. 2006 NSTI Nanotechnology conference and trade show, Boston, MA, pp 546–549
- Wang Y, Lin Q, Mukherjee T (2006b) Composable behavioral models and schematic-based simulation of electrokinetic lab-on-a-chip systems. *IEEE Trans Comput Aided Des Integr Circuit Syst* 25(2):258–273
- Wang Y, Mukherjee T, Lin Q (2006c) Systematic modeling of microfluidic concentration gradient generators. *J Micro-mech Microeng* 16(10):2128–2137
- White FM (1991) *Viscous fluid flow*. McGraw-Hill, New York
- Wouwer AV, Saucez P, Schiesser WE (2004) Simulation of distributed parameter systems using a Matlab-based method of lines toolbox: Chemical engineering applications. *Ind Eng Chem Res* 43(14):3469–3477
- Xuan X, Li D (2004) Analysis of electrokinetic flow in microfluidic networks. *J Micromech Microeng* 14(2):290–298
- Zhang T, Chakrabarty K, Fair RB (2004) Behavioral modeling and performance evaluation of microelectrofluidics-based PCR systems using SystemC. *IEEE Trans Comput Aided Des Integr Circuit Syst* 23(6):843–858